

Finite element analysis of cone penetration in cohesionless soil

W. Huang ^{a,*}, D. Sheng ^a, S.W. Sloan ^a, H.S. Yu ^b

^a *Discipline of Civil, Surveying and Environmental Engineering, University of Newcastle, Callaghan, NSW 2308, Australia*

^b *School of Civil Engineering, University of Nottingham, Nottingham NG7 2RD, UK*

Received 21 June 2004; received in revised form 10 August 2004; accepted 6 September 2004

Abstract

Displacement finite element analysis is performed for a cone-penetration test in cohesionless soils. By modelling finite strain in the soil and large scale sliding at the penetrometer–soil interface, a more realistic penetration process is simulated in which the penetrometer is assumed to be rigid and the soil is assumed to be an elastic-perfect-plastic continuum obeying the Mohr–Coulomb criterion. The cone resistance found from the calculations shows that the depth of steady-state penetration depends on the stress state and the soil properties. Parametric studies are performed to illustrate the influence of various factors on the cone resistance at the steady state. The deformation mode of the soil around the cone, as well as the plastic zone, is shown to be similar to that caused by cavity expansion. Indeed, the calculated cone resistances are comparable with empirical correlations based on cavity-expansion theory.

© 2004 Elsevier Ltd. All rights reserved.

Keywords: Cone penetration; Cohesionless soil; Finite element analysis; Cone resistance

1. Introduction

The cone-penetration test (CPT) is widely used in geotechnical engineering for in situ soil tests. In a CPT, a cone-shaped penetrometer of a standard geometry is pushed into the ground at a constant rate while the resistance on the cone is measured. The sleeve friction on the shaft is often recorded as well. In the piezocone penetrometer, pore pressure is typically measured at one, two, or three locations on the cone or the shaft. Using the CPT to probe soil stratigraphy has been practised since 1917. Nowadays, the CPT is also applied for soil classification and soil property estimation.

To determine soil properties from measured cone data, it is necessary to establish some relations among them. For this purpose, much previous work has fo-

cused on cone-penetration analysis over the past two decades (see e.g. [21,14,18,24]). The difficulties lie in the complicated deformation of the soil, which results from the punching of the penetrometer, as well as the complex interfacial behaviour. Rigorous closed form solutions are not available for penetration problems, and analyses are often based on simplified theories. One approach treats the steady-state penetration of the cone as a limit equilibrium problem of a circular footing, and proposes correlations based on its bearing capacity (e.g. [5,9,15,11,4]). The applicability of correlations of this type is limited due to the assumption that soil compressibility and elastic deformation are negligible. Another type of correlation often used in practice is based on the solutions of cavity expansion theory (e.g. [13,20,23,16]). This approach includes parameters related to soil deformation, and is therefore more flexible for applications.

Various numerical methods have also been employed to model cone-penetration analysis. While these

* Corresponding author. Tel.: +61 2 4921 6082; fax: +61 2 4921 6991.

E-mail address: wenxiong.huang@newcastle.edu.au (W. Huang).

do not always provide straightforward correlations, they do provide a better understanding of the penetration process, a check of the factors affecting the cone resistance, and a verification of empirical relations. Because cone penetration involves finite deformation of the soil and large-scale sliding at the penetrometer–soil interface, rigorous numerical modelling of it is rather difficult and various approximations are often adopted. For instance, [3] performed finite element analysis of cone penetration but assumed small strains. Previous to this, the strain path method for steady state analysis of cone penetration was employed by Baligh [1] and Houlsby et al. [10]. In this type of analysis, the pattern of deformation is prescribed without necessarily satisfying the equilibrium conditions. Special finite element procedures for steady-state analysis, which neglect the transient component of the deformation, have been developed by Herrmann and Mello [7] and Yu et al. [25]. In all these finite element analyses, the penetrometer was assumed to be pre-placed in the soil with a borehole, and only a limited number of penetration steps could be modelled. Even when the finite element analysis allows for finite strain [6,12], modelling the whole penetration process is not possible unless large-scale sliding is permitted at the penetrometer–soil interface. More recently, [17] presented finite element analysis of cone penetration in cohesive soils. Contact elements, capable of finite sliding along the penetrometer surface, were used to model the whole penetration process from the ground surface to any depth. The emphasis of their study was on pore-pressure development around the cone under different penetration speeds.

This paper presents a finite element analysis of cone-penetration tests in cohesionless soil, focusing on the penetration mechanism and the factors affecting the cone resistance. The analysis is based on a rigorous numerical simulation of the penetration process. The penetrometer is idealised as a rigid body, and the soil as an elastic-perfect-plastic material. The Mohr–Coulomb failure criterion is adopted for plastic yielding. A frictional contact element, which allows finite sliding, is used in the nonlinear finite element analysis, so that the complete penetration process (up to and including the steady state condition) is modelled realistically. The cone resistance is obtained by dividing the reaction force acting on the rigid cone by its base area. The steady state is then determined from the evolution of cone resistance. Sensitivity of the steady state cone resistance to the stress state and material parameters is examined through parametric studies. The deformation mode in the soil around the cone is also studied and compared with cavity-expansion theory. Finally, the numerical results are compared with empirical correlations and their discrepancies are discussed.

2. Modelling of the problem

2.1. Frictional sliding at the soil-cone interface

The cone-penetration process involves punching of the penetrometer into the soil, which is pushed both sideways and downwards, and finite sliding along the soil–penetrometer interface. Significant deformation can be observed in the soil around the penetrometer as the soil is pushed aside to make room for it. Since the penetrometer deformation is negligible, it is reasonable to treat it as a rigid body. For a rigorous finite analysis, simulation of the interface with finite sliding plays a key role. In this study, the commercial finite element program ABAQUS is used for the finite element calculations, and finite sliding is modelled using a frictional contact interface. The software uses the concept of a ‘master surface’ and a ‘slave surface’, with the former being able to penetrate the latter. The iterative algorithm for implementing this behaviour consists of searching for contact nodes and applying contact forces between the slave and master surfaces. For the present problem, the surface of the rigid body is defined as being the master surface, while the potential contact surface in the soil body is deemed to be the slave surface.

The pressure force applied on the contact node depends on the overclosure of penetration h , which is defined by:

$$\mathbf{n}h = -\mathbf{x}_A + \mathbf{x}_C + \mathbf{r}, \quad (1)$$

where \mathbf{x}_A denotes the coordinate vector of node A on the slave surface, \mathbf{x}_C is the coordinate vector of a reference node C on the rigid body, \mathbf{r} is the vector from node C to point A' (which is the ‘anchor’ point of node A on the master surface), and \mathbf{n} is the normal vector on the master surface at A' along $A'A$ (see Fig. 1). Note that the ‘anchor’ point A' is not necessarily a node, it is only a point on the master surface closest to node A . In the present study, the so-called hard contact condition is assumed

$$h \leq 0, \quad p_n \geq 0, \quad p_n h = 0. \quad (2)$$

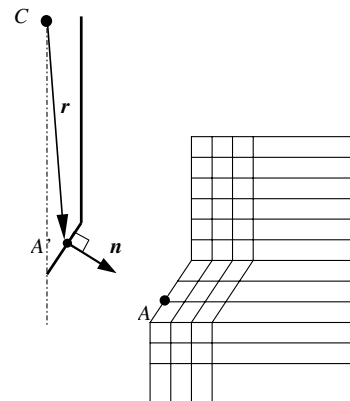


Fig. 1. Sketch of contact interface.

Herein, p_n represents the contact pressure. Node A on the slave surface is considered to be in contact with the master surface only when $h = 0$ & $p_n > 0$. The contact constraint is enforced with a Lagrangian multiplier, which represents the contact pressure in a mixed formulation [8].

Sliding can occur if a node on the slave surface is in contact with the master surface. In this case, a critical shear stress can be calculated, based on the friction law $\tau_{crit} = p_n \cdot \tan \phi_{sc}$, where ϕ_{sc} denotes the frictional angle on the penetrometer–soil interface. A contact node is in a “sticky” state as long as the actual shear stress τ is less than τ_{crit} , and an elastic response is assumed. Otherwise, the contact node undergoes sliding, which is a perfectly-plastic response.

2.2. Modelling of soil behaviour

A large number of constitutive models exist for different soils. To capture as many aspects of soil behaviour as possible, some of these are very sophisticated and involve lots of parameters. However, in engineering practice, simple models are often sufficient as only the key features of soil behaviour are of importance. In this study, a simple elastic-perfect-plastic model with the Mohr–Coulomb yield criterion is used to describe the behaviour of a cohesionless soil. The elastic deformation is described by the elastic modulus E (or the shear modulus G) and the Poisson’s ratio ν , while the plastic deformation is characterized by the friction angle ϕ , the dilation angle ψ , and the cohesion c ($c \approx 0$ for a cohesionless soil). A non-associated flow rule is used to simulate the dilatant behaviour of the soil.

A real cohesionless soil often exhibits density-dependent behaviour. In response to large shear deformation, the mobilized friction angle tends to a stationary value (usually denoted by ϕ_c) which is known as the critical friction angle. Peak strengths followed by softening are observed only in initially dense sands. The present elastic perfectly-plastic soil model has the soil friction and dilation angles as two independent parameters. The critical state value is taken for the friction angle ($\phi = \phi_c$), with the density effect being reflected by the dilation angle. For the case where the peak friction angle is considered, it may be related to the dilation angle ψ through Bolton’s relation [2]

$$\phi_p = \phi_c + 0.8\psi. \tag{3}$$

2.3. Displacement finite element analysis

Displacement finite element analyses are performed with geometric nonlinearity being taken into account. Cauchy stress and the symmetric part of the velocity gradient (also known as the stretching tensor) are used to define the stress and strain rate in the deforming soil.

Equilibrium is checked on the current configuration and a standard Newton iteration procedure is applied to solve the governing nonlinear system of equations.

Cohesionless sandy soils, with a relatively large permeability, are considered so that any excess pore pressure developed during the penetration process can be neglected, and a fully drained condition is assumed.

In the numerical calculations, a standard penetrometer geometry is used — that is, a penetrometer with a shaft diameter of $d_c = 35.7$ mm and a tip angle of $\alpha = 60^\circ$. The soil domain is modelled by an axi-symmetric mesh of 1 m radius (about 56 times that of the cone radius) and 2 m depth, with 1600 8-noded biquadratic elements (Fig. 2). The grid is so designed that the elements potentially in contact with the cone have a size of about one-third of the cone radius. The element size is increased both horizontally and vertically from the penetrometer to control the total number of equations to be solved. Test runs have shown that further refinement of the mesh has no significant influence on the numerical results.

Due to the large number of degrees of freedom in the mesh, as well as the material and geometric nonlinearities, simulation of a very deep penetrometer would require a huge amount of CPU time. This problem is overcome by applying a vertical overburden pressure p_0 on the top boundary of the mesh to represent the stress state at a specific depth. The nodes on the bottom boundary are fixed, while the nodes on the right-hand side are allowed to move vertically. The left boundary

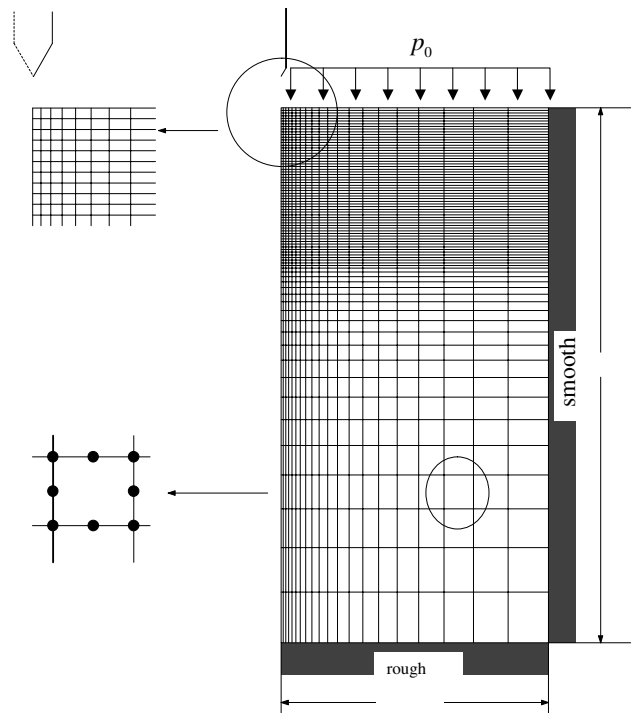


Fig. 2. Finite element mesh for analysis.

is the axis of symmetry. The initial stress state is characterized by the overburden pressure p_0 and the lateral earth pressure coefficient K_0 only. The self-weight of the soil in the computation domain is not included, so as to give better control of the vertical stress (which is specified and models the effect of gravity). This omission of the self-weight does not change the penetration mechanism and, therefore, will not significantly affect the normalized cone resistance. Indeed, this approach simplifies the treatment of the calculated cone factors and can lead to a better estimation of the so-called steady state (which is characterized by a constant cone resistance instead of a linearly increasing cone resistance). Initially, the cone is located on the top boundary and the penetration process is simulated by applying a vertical displacement to it. In all numerical calculations, the soil cohesion c is set to zero and Poisson's ratio is fixed at 0.3. Parametric studies are performed to investigate the influence of the pressure level p_0 , the shear modulus G , the soil internal friction angle ϕ , and the dilation angle ψ .

3. Evolution of cone resistance and interfacial friction

The reaction force during penetration, obtained from the numerical calculations, represents the total pushing force acting on the penetrometer. This total pushing force, denoted by F_t , is equal to the sum of the resistance force on the cone, F_c , and the friction force on the shaft, F_s , i.e.

$$F_t = F_c + F_s \tag{4}$$

In Fig. 3, numerical results are shown for the evolution of the total pushing force F_t obtained for different penetrometer–soil interface friction angles ϕ_{sc} . Two phases can be observed in these evolution curves. The first phase corresponds to a strongly nonlinear variation in F_t as the depth of penetration z increases. The interfacial friction angle ϕ_{sc} has only a minor influence during this transient phase. The second phase starts at a critical penetration depth z_c , and is characterised by a

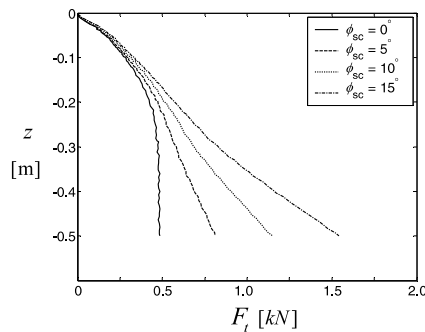


Fig. 3. Evolution of total reaction force acting on the rigid body for various interfacial frictions ($\phi = 30^\circ$, $\psi = 10^\circ$, $G/p_0 = 100$, $p_0 = 10$ kPa, $K_0 = 1.0$).

nearly linear increase in the total pushing force with z . The greater the interfacial friction, the faster the increase in the total pushing force. It is notable that the total pushing force F_t remains almost constant for $\phi_{sc} = 0$. Therefore, the second phase corresponds to the so-called steady state. Small numerical oscillations are observed in the evolution curves for F_t . The critical depth z_c was found to be related to the size of the plastic zone in the soil which, in turn, depends on the stress state and the soil properties.

Penetrometers are usually designed to allow the cone resistance, and sometimes the sleeve friction, to be measured. The former is the most important quantity for engineering design, and is defined as

$$q_c = 4F_c/\pi d_c^2, \tag{5}$$

where d_c is the shaft diameter of the cone. As only F_t in Eq. (2) can be obtained directly from finite element calculations, it is necessary to identify the cone resistance force F_c separately. To achieve this end, the interfacial friction ϕ_{sc} was set to zero in the finite element calculations. Thus the obtained total reaction force is the same as the resistance force on the cone, i.e. $F_c|_{\phi_{sc}=0} = F_t|_{\phi_{sc}=0}$. Note that, for a non-zero interface friction angle, the interfacial friction on the cone tip makes a contribution to the actual cone resistance. By neglecting it, only the nominal cone resistance $\bar{q}_c = q_c|_{\phi_{sc}=0}$ is obtained through Eq. (5).

To account for the contribution of interfacial friction to the total cone resistance, the nominal cone resistance can be multiplied by a tip friction factor, η , so that

$$q_c = \eta \bar{q}_c. \tag{6}$$

The tip friction factor η is estimated analytically by considering simple equilibrium of the cone (refer to Fig. 4). With the presence of interface friction, the total cone resistance force can be expressed as

$$\begin{aligned} q_c A_c &= \int_{A'_c} p_n (\sin(\alpha/2) + \cos(\alpha/2) \tan \phi_{sc}) dA'_c \\ &= (\sin(\alpha/2) + \cos(\alpha/2) \tan \phi_{sc}) \int_{A'_c} p_n dA'_c, \end{aligned}$$

where A'_c represents the tip area and α the tip angle of the cone. By setting $\phi_{sc} = 0$ we have $\bar{q}_c A_c = \sin(\alpha/2) \int_{A'_c} p_n dA'_c$. Under finite strain conditions, changing the

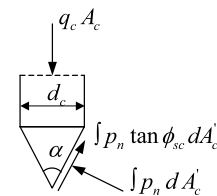


Fig. 4. Illustration of contribution of the interface friction to the cone resistance.

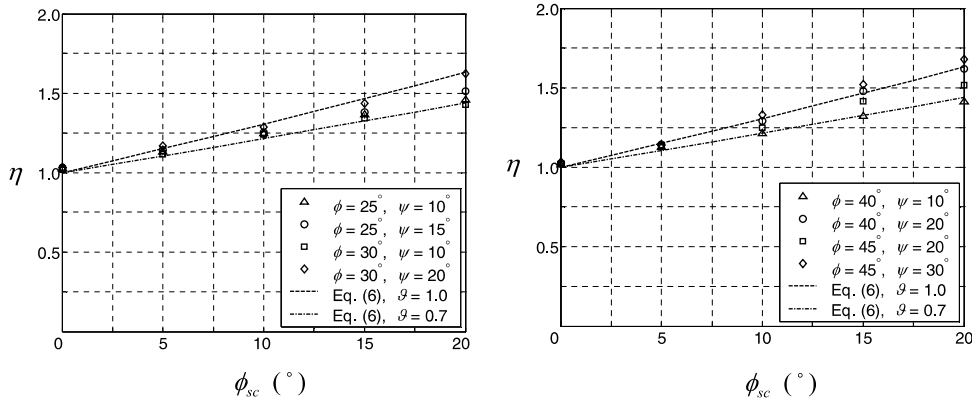


Fig. 5. Numerical and analytical results for the cone tip friction factor.

interface friction may have some influence on the normal contact pressure p_n . By neglecting such an influence, a representation for the friction factor can be obtained from the ratio $q_c A_c / \bar{q}_c A_c$

$$\eta = 1 + \cot(\alpha/2) \tan \phi_{sc}. \tag{7}$$

For a standard cone with $\alpha = 60^\circ$, Eq. (7) becomes $\eta = 1 + \sqrt{3} \tan \phi_{sc}$.

Since representation (7) is only an approximation for the tip friction factor, a number of numerical tests were performed with interface friction angles of $\phi_{sc} = 0^\circ, 5^\circ, 10^\circ, 15^\circ$ and 20° (Fig. 3). Once the steady state was reached for a given penetration depth, the shaft friction force F_s was computed by integrating the shear stress along the interface. The tip friction factor was then calculated according to $\eta = (F_t - F_s) / F_t|_{\phi_{sc}=0}$. It was found that the numerical results may deviate from Eq. (7) and are slightly influenced by the dilation angle ψ as shown in Fig. 5. To fit the numerical results, Eq. (7) needs to be modified according to

$$\eta = 1 + \vartheta \cot(\alpha/2) \tan \phi_{sc}, \tag{8}$$

where ϑ ranges from 0.7 to 1.1. For the numerical CPT data, Eq. (8) gives a reasonable estimate of the

tip friction factor with $\vartheta = 0.86$, which is a least squares fit.

4. Cone resistance at steady states

Cone resistance is influenced by many factors-including the soil stress state, the soil shear modulus, the soil friction angle, and the soil dilation angle. In this section, the effect of each of these factors is examined separately. The cone resistance for steady states is obtained by checking the evolution of the cone resistance from numerical calculations with $\phi_{sc} = 0$.

Figs. 6(a) and (b) show, respectively, the effect of the vertical pressure p_0 on the evolution of the mobilized cone resistance and the steady state cone resistance q_c . The former plot demonstrates that the steady state is reached sooner at higher stress levels (larger values of p_0), while the latter plot shows that the steady state value of q_c increases linearly as p_0 increases. Note, however, that q_c does not vanish as p_0 approaches zero. This can be explained by the fact that a reactive stress field is built up in the soil upon the initial penetration of the cone.

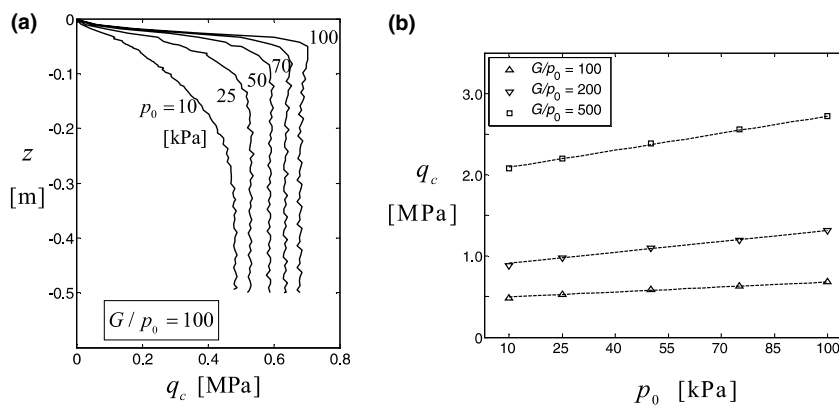


Fig. 6. (a) The evolution of cone resistance and (b) variation of cone resistance at steady states for various values of p_0 ($\phi = 30^\circ, \psi = 10^\circ, K_0 = 1.0, \phi_{sc} = 0$).

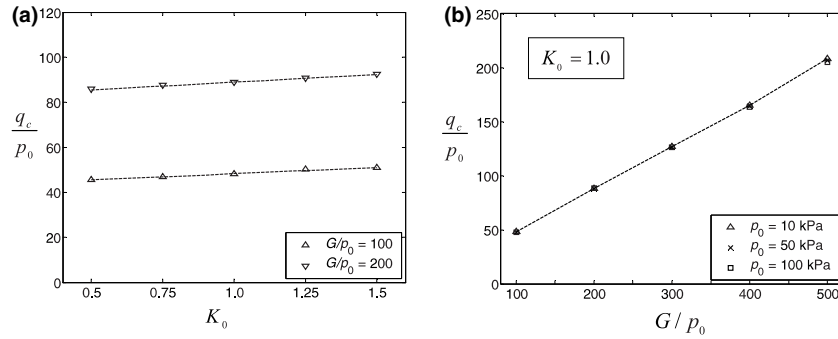


Fig. 7. Normalised cone resistance versus (a) lateral pressure coefficient K_0 and (b) ratio G/p_0 ($\phi = 30^\circ, \psi = 10^\circ, \phi_{sc} = 0$).

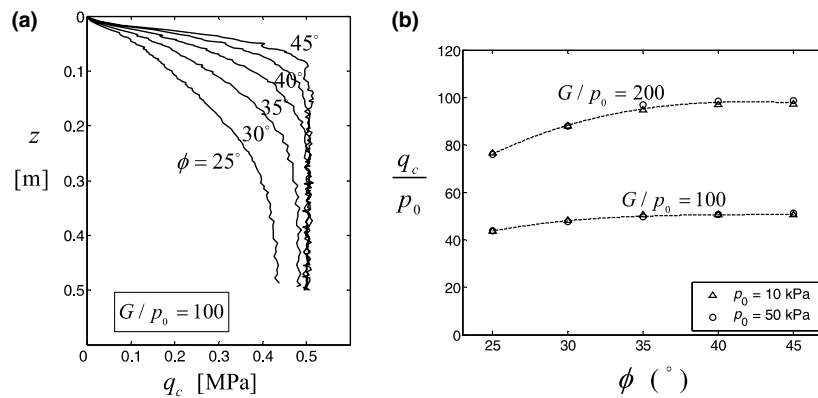


Fig. 8. (a) Evolution of cone resistance and (b) cone resistance at steady states for various friction angles ($\psi = 10^\circ, K_0 = 1.0, \phi_{sc} = 0$).

The horizontal stress is controlled by the lateral stress coefficient K_0 , whose effect is shown in Fig. 7(a). A nearly linear relation is obtained between q_c and K_0 . As K_0 increases from 0.5 to 1.5, the initial horizontal stress increases at the same rate. However, the increase in the corresponding cone resistance is relatively small. The influence of shear modulus G is significant, as can be seen in Fig. 6(b) and Fig. 7. Further studies show that this effect is coupled with the stress level, and that the cone resistance can be related to the ratio G/p_0 . By fix-

ing the ratio G/p_0 it was found that the normalised cone resistance q_c/p_0 is almost independent of the stress level (Fig. 7(b)).

Figs. 8 and 9 shows the dependence of the cone resistance on the soil friction angle ϕ and dilation angle ψ , respectively. The influence of the former is examined over a range of 25–45°, and it can be seen that q_c increases with ϕ . This effect is most obvious for $25^\circ \leq \phi \leq 35^\circ$ and for a higher ratio of G/p_0 . As ϕ varies from 35° to 45°, the corresponding cone resistance at the

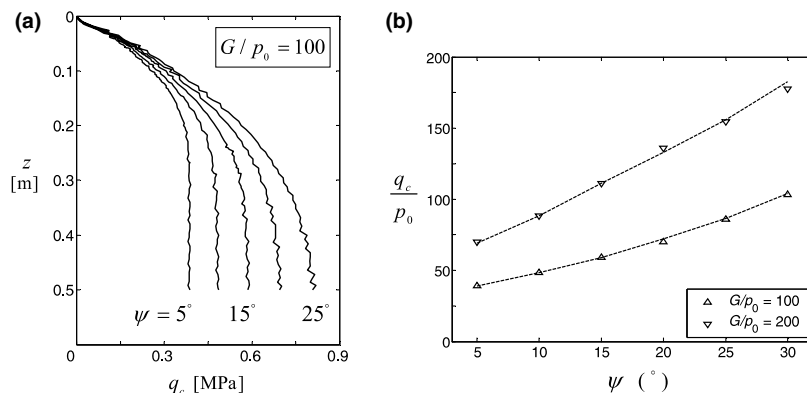


Fig. 9. (a) Evolution of cone resistance and (b) cone resistance at steady states for various dilation angles ($\phi = 30^\circ$ and $K_0 = 1.0, \phi_{sc} = 0$).

steady state varies only slightly, even though the transient responses are rather different (Fig. 8(a)). This could be related to the fact that cone penetration is basically a deformation controlled test. As the total deformation is fixed, an increase in the yield limit is accompanied by a decrease in the size of the plastic zone and only a slight increase in the cone resistance. In contrast, varying the angle of dilation has a pronounced effect on the cone response. Increasing ψ leads to an obvious increase in cone resistance, with deeper penetration being needed to reach the steady state. This result stems from dilation in the plastic zone, which increases the mean pressure and hence the cone resistance.

5. Soil deformation and plastic zone

Penetration of a cone into the ground involves pushing the surrounding soil downwards and sideways. The process can be clearly understood by viewing the deformed mesh and displacement field in the soil around the penetrometer, as shown in Fig. 10. It can be seen that the soil particles on the axis of symmetry move only vertically downwards, whereas soil particles in contact with the cone surface are pushed sideways as well. From the cone tip to the shaft, the horizontal displacement of soil particles increases, with the maximum horizontal displacement being observed at the edge of the cone. This maximum displacement is controlled by the diameter of the penetrometer shaft. If only the horizontal displacement is considered, the penetration process resembles a cylindrical cavity expansion to a limited radius. The vertical displacement component exists due to the inclined surface of the cone and the interface friction. By looking at a plot of the plastic zone around the penetrometer (Fig. 11), we can see that its shape differs from those predicted by cylindrical or spherical cavity expansion theory [20,16]. These plots indicate that the plastic zone enlarges and moves downwards as the

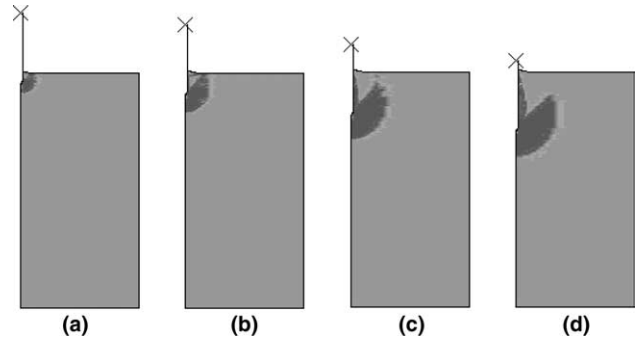


Fig. 11. Plots of the plastic zone at different depths of penetration: (a) $2.5 d_c$; (b) $5.1 d_c$; (c) $10.2 d_c$; (d) $14.0 d_c$, with d_c being the cone diameter ($G/p_0 = 100$, $\phi = 30^\circ$, $\psi = 10^\circ$).

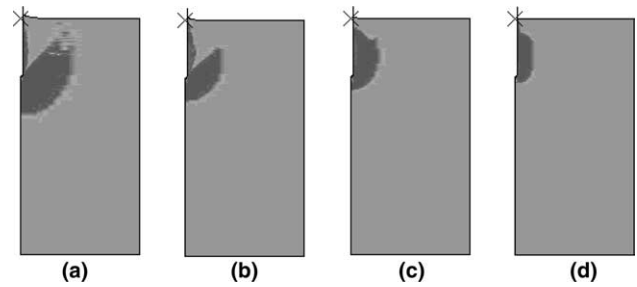


Fig. 12. Plots of the steady state plastic zone for: (a) $p_0 = 10$ kPa; (b) $p_0 = 25$ kPa; (c) $p_0 = 50$ kPa; (d) $p_0 = 100$ kPa ($G = 2000$ kPa, $\phi = 30^\circ$, $\psi = 10^\circ$).

cone is inserted in the soil. It ceases to grow once the cone reaches the steady state penetration depth. This depth is reached earlier for cases where the size of the stable plastic zone is smaller. Fig. 12 shows plots of the steady state plastic zone for various values of initial pressure. It can be seen that the size of the plastic zone decreases as the initial pressure increases.

The shape of the moving plastic zone around the cone tip resembles that of half an ellipse, with the longer axis

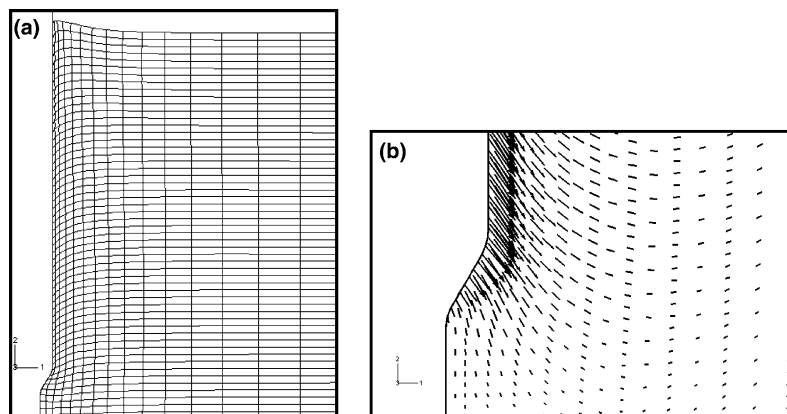


Fig. 10. (a) Deformed mesh and (b) displacement field around the cone at a steady state.

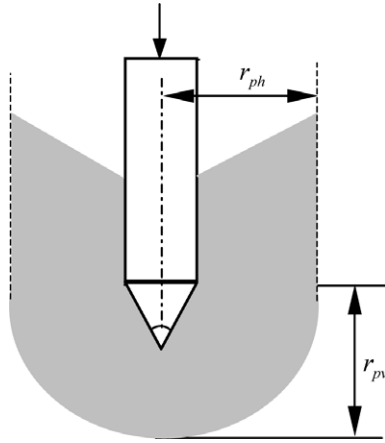


Fig. 13. Sketch of plastic zone around the cone; its size is given by $r_p = (r_{ph} + r_{pv})/2$.

being aligned in the horizontal direction, as sketched in Fig. 13. The dependence of the steady state size of the plastic zone on the soil parameters and stress state is presented in Fig. 14. In this plot, the size of the plastic zone is characterised by the quantity r_p , which is obtained by averaging its horizontal and vertical dimensions.

It was found that the size of the plastic zone decreases by a factor of approximately 4 as the initial mean pressure p_0 is increased by a factor of 10, as shown in Fig.

14(a). This can be related to the displacement-controlled deformation mode in the soil. An increase in the mean pressure leads to a higher yield stress. Because the total deformation required to make room for the cone is more or less fixed, the plastic deformation is thus expected to be smaller. In contrast, with a higher shear modulus (i.e. a stiffer soil), a smaller portion of the total deformation is elastic. Therefore, the size of the plastic zone r_p increases significantly as the ratio G/p_0 increases. Fig. 14(b) indicates that r_p increases by a factor of approximately 2 as G/p_0 increases from 100 to 400. It is worth noting that, if the ratio G/p_0 is kept constant, r_p varies very little as either the mean pressure or the shear modulus changes. Therefore, the effects of the shear modulus more or less offset the effects of the mean stress.

Fig. 14(c) shows that the size of the plastic zone r_p decreases as the friction angle ϕ increases. This is due to the fact that an increase in ϕ also leads to an increase in the yielding stress. As the total deformation required to make room for the cone is more or less fixed, the increase in strength will result in a decrease in the plastic deformation. Fig. 14(c) indicates that r_p decreases by a factor of approximately 1.6 as ϕ increases from 25° to 45° . In contrast, the size of the plastic zone r_p almost doubles as the dilation angle ψ increases from 5° to 25° (Fig. 14(d)). This is also in agreement with the general observation that less deformation is required to reach plastic yielding in a more dilatant soil.

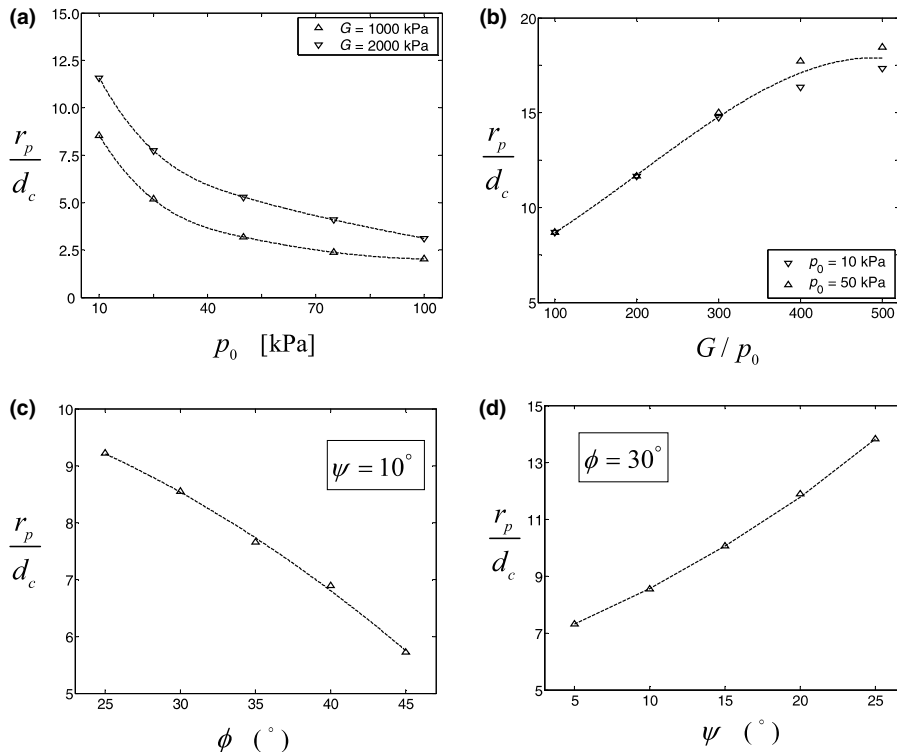


Fig. 14. Variation in the size of the plastic zone with respect to: (a) stress; (b) shear modulus; (c) friction angle; (d) angle of dilation.

6. Comparison with empirical correlations

In the parametric study presented above, only one soil parameter is varied each time. This is rarely true for real soils. Therefore, the correlations between the cone resistance and each of the soil parameters might not apply in practice. However, numerical studies can provide a proper assessment of existing empirical correlations. Most of these correlations fall into two categories: those which are based on the solution of bearing-capacity problems, and those which are based on the theory of cavity expansion.

Empirical correlations of the first category are usually expressed in simple forms that relate the friction angle with cone resistance – as, for instance, in the correlation proposed by Robertson and Campanella [15], which reads

$$q_c/p_0 = C_2 \exp[C_1 \tan \phi] \tag{9}$$

with $C_1 = 6.820$ and $C_2 = 0.266$. In bearing-capacity analysis, only the limit equilibrium state of collapse is considered, with the soil compressibility and soil deformation being neglected. However, cone penetration is more of a displacement-controlled steady deformation process than a limit equilibrium problem. The compressibility of the soil has a strong influence on the cone resistance, which is not reflected by this type of correla-

tion. Therefore the applicability of this type of correlation is limited.

The comparison between the finite element results (dashed curves) and the prediction of Eq. (9) (solid curves) is presented in Fig. 15. In these plots the cone resistances from finite element calculations have been adjusted by multiplying the tip friction factor η given in Eq. (8) for $\phi_{sc} = 10^\circ$. Significant differences between the numerical and empirical correlations can be seen. Since the dilation angle is not explicitly included in Eq. (9), comparison is made for a fixed dilation angle $\psi = 10^\circ$ (Fig. 15(a)), for an associated flow rule with $\psi = \phi$ (Fig. 15(b)), and by setting $\phi = \phi_p$ in Eq. (9), which is related to the variation of dilation angle via Bolton’s relation (3) with $\phi_c = 30^\circ$.

Empirical correlations of the second category are often in a more complicated form, as they depend on solutions to cavity expansion problems. In fact, closed form analytical solutions are not always available, particularly for the Mohr–Coulomb yield criterion with a non-associated flow rule. Vesic [19] presented a simplified solution for cavity expansion in infinite Mohr–Coulomb soil. Based on this solution, he proposed a correlation for cone resistance, which reads [20]:

$$\frac{q_c}{p_0} = \frac{1 + 2K_0}{3 - \sin \phi} \exp[(\pi/2 - \phi) \tan \phi] \tan^2(\pi/4 + \phi/2) I_{rr}^n, \tag{10}$$

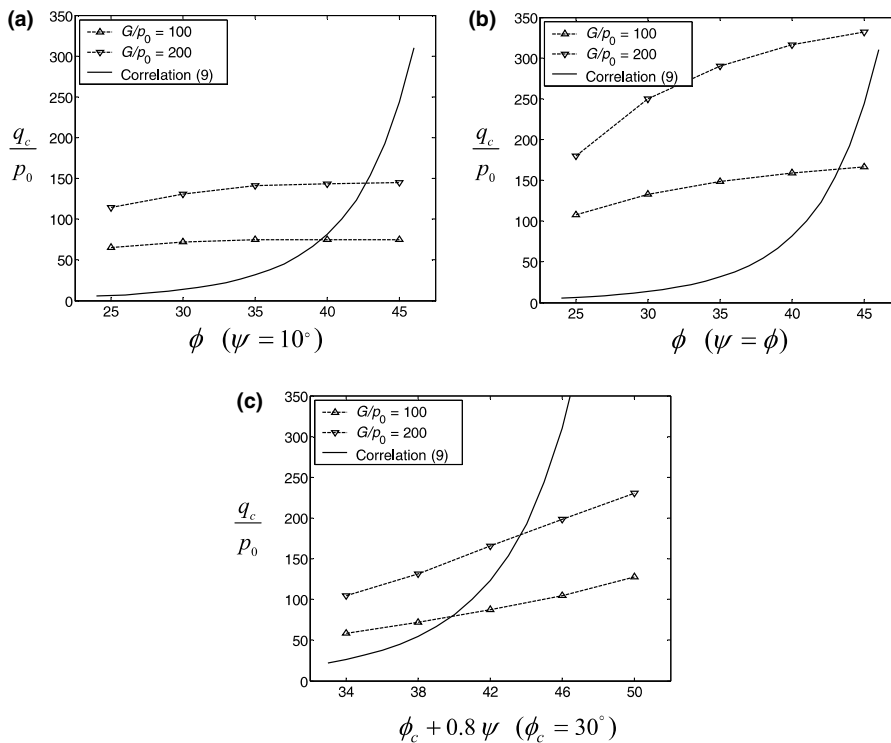


Fig. 15. Comparison of correlation (9) (solid curves) with numerical results (dashed curves) for: (a) various friction angles with dilation angle $\psi = 10^\circ$; (b) various friction angles with associate flow; (c) various peak friction and dilatancy angles given through Bolton’s relation (3).

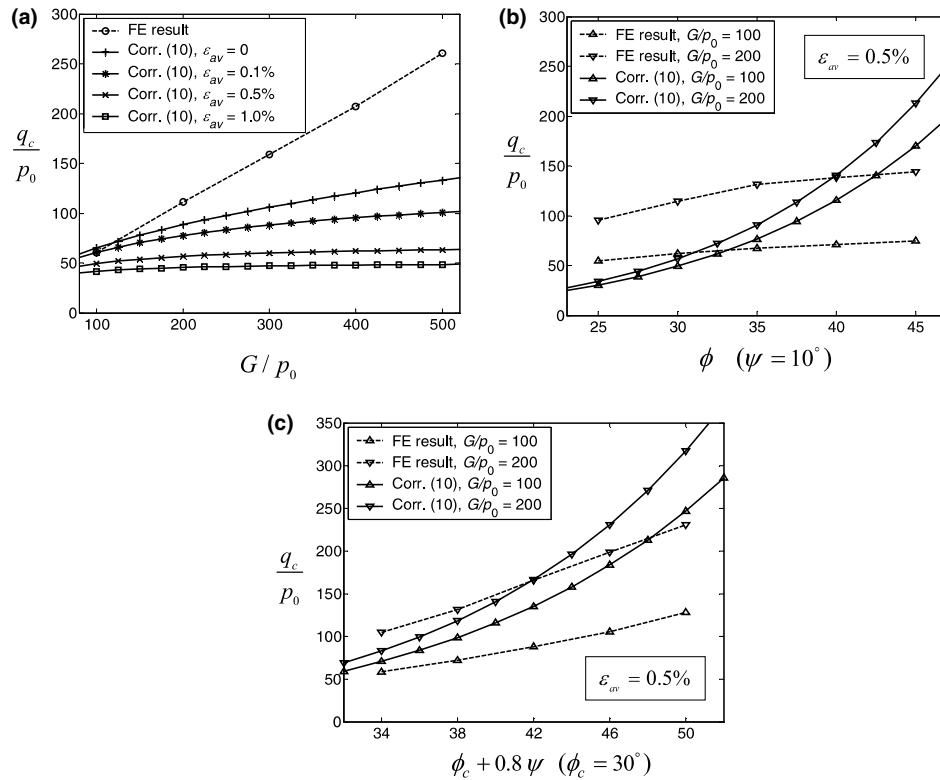


Fig. 16. Comparison of correlation (10) (solid curves) with finite element results (dashed curves) for: (a) various ratios of shear modulus to stress; (b) various friction angles with a constant dilation angle; (c) various peak friction and dilation angles given through Bolton's relation (3).

where I_{rr} is called the 'reduced rigidity index' and is a modification of the so-called 'rigidity index' I_r . The parameters I_{rr} , I_r and n are defined as

$$I_{rr} = \frac{I_r}{1 + \varepsilon_{av} I_r}, \quad I_r = \frac{G}{p_0 \tan \phi + c}, \quad n = \frac{4 \sin \phi}{3 + \sin \phi},$$

where ε_{av} represents the average volumetric strain in the plastic zone. Actually ε_{av} in the correlation is an unknown factor, which is related to the size of the plastic zone and the mechanical parameters of the soil. Prediction of ε_{av} is a task not much easier than the prediction of the cone resistance itself. In Fig. 16, numerical results (dashed curves) are compared with the prediction of correlation (9), with an assumed value of ε_{av} (solid curves).

The dependence of cone resistance on the ratio G/p_0 is shown in Fig. 16(a) for $\varepsilon_{av} = 0, 0.1\%, 0.5\%$, and 1% . We can see that the numerical results (dashed line) indicate a much stronger dependence of the cone resistance on the elastic modulus of the soil than the correlation does. And the dependence of the cone resistance on the friction angle from the correlation is roughly in agreement with the numerical results (Fig. 16(b)). On the other hand, a reasonable agreement between the correlation and the numerical prediction is obtained for the effect of the angle of dilation (Fig. 16(c)). In Vesic's solution, the effect of dilation angle is taken into account implicitly through the average volumetric strain ε_{av} . In Fig.

16(c), the curves from the correlation are obtained by assuming a constant value for ε_{av} , since the variation of ε_{av} with respect to ψ is not specified. Qualitatively, ε_{av} increases with ψ , which corresponds to a decrease of the reduced rigidity. This, in turn, will result in a better agreement between the correlation and the numerical prediction.

Yu and Houlsby [22] provided a semi-analytical solution for spherical and cylindrical cavity expansion in Mohr–Coulomb frictional soil with a non-associated flow rule. The solution is expressed in a series form, from which the limit pressure can be computed through a simple numerical procedure. The cone resistance q_c may be approximately related to the limit pressure from spherical cavity expansion, p_s , in the following form [23]:

$$q_c/p_0 = (1 + \sqrt{3} \tan \phi) p_s/p_0. \quad (11)$$

By computing the limit pressure factor p_s/p_0 , the correlation (11) is compared with finite element results in Fig. 17. It can be seen that the correlation under-estimates the effect of the elastic shear modulus (Fig. 17(a)), but overestimates the effect of the soil friction angle (Fig. 17(b) and (c)). The predicted dependence of the cone resistance on the angle of dilation, however, is in reasonable agreement with the numerical prediction (Fig. 17(d)).

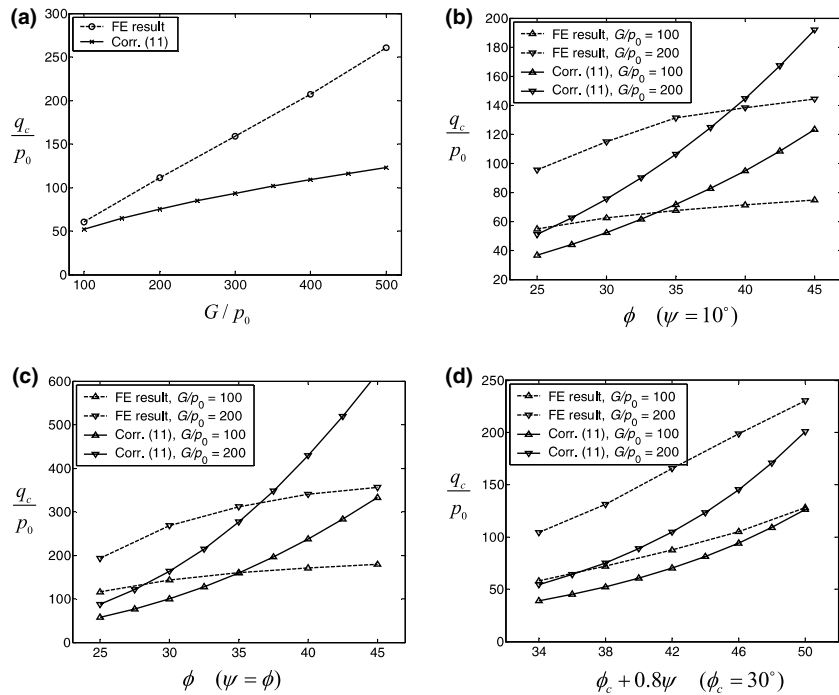


Fig. 17. Comparison of correlation (11) based on Yu and Housby solution (solid curves) with finite element results (dashed curves) for: (a) various ratios of shear modulus to stress; (b) various friction angles with a constant dilation angle; (c) various friction angles with associated flow; (d) various peak friction and dilation angles given through Bolton's relation (3).

Generally speaking, the cone-penetration process is closer to being a cavity-expansion problem than to being a bearing-capacity problem. If only the horizontal displacement of the soil around the cone is considered, the penetration process is similar to a cylindrical cavity expansion. However, with consideration of the vertical displacements in the soil around the cone and within the plastic zone, the degree of similarity becomes unclear. In addition, in cavity-expansion theory, the limit pressure for cavity expansion is usually used for correlation with the cone resistance. The limit pressure in a cavity expansion corresponds to a state in which the pressure does not change with further expansion of the cavity, a state that can be approached asymptotically with a very large expansion. In the cone-penetration process, the soil particles around the cone might not reach such a large displacement. As the cone tip cuts into the soil, and as sliding occurs at the interface, the vertical displacements of the soil particles are limited. The horizontal displacements of these particles are also limited (they are controlled by the diameter of the penetrometer shaft). Consequently, the stress state in the soil around the cone surface might not approach the limit pressure, as assumed in cavity-expansion theory. The fact that the size of the plastic zone decreases with increasing friction angle also indicates that the limit pressure is not approached in the cone-penetration process. This fact explains why correlations based on cavity expansion theory underestimate the effect of the elastic

modulus, but overestimate the effect of the friction angle, on the cone resistance.

7. Conclusion

Simulating the process of cone penetration rigorously depends on accurate modelling of both the soil and interface behaviour. By including finite deformation of the soil and large scale sliding at the penetrometer–soil interface, the complete penetration process, starting from the ground surface, can be modelled. It has been shown that steady states can be observed following a transient period of penetration. The penetration depth of the transient phase is related to the steady state size of the plastic zone developed around the cone and the shaft. The size of this zone depends on the stress state and soil deformation parameters, as well as strength parameters.

In a cone-penetration test, soil around the cone is pushed downwards and outwards to accommodate the penetrometer. The horizontal displacement of soil particles around the cone is controlled by the size of the penetrometer shaft, whereas the vertical displacement depends on the elastic properties of the soil, the friction at the conesoil interface, and the strength of the soil. The true deformation pattern around a penetrating cone is somewhat different from that assumed in bearing-capacity theory or cavity-expansion theory. This is because the soil around the cone or shaft does not necessarily

approach the limit strength state. Parametric studies show that the cone resistance is influenced more by deformation properties (such as shear modulus and angle of dilation) than by shear strength parameters (such as the friction angle).

Comparatively, steady state penetration is more similar to a cavity expansion problem than a bearing capacity problem. A preliminary comparison presented in this paper suggests that a reasonable agreement has been obtained between the numerical results and correlations based on cavity expansion theory. It has also been found that most empirical correlations tend to underestimate the influence of elastic modulus and overestimate the influence of the friction angle, particularly for compressible soils.

Although a more realistic penetration process is modelled in this study, the current work has been focused on the cone resistance and did not use the computed values of sleeve friction. This is mainly because a homogeneous soil is considered and an assumed interface friction is applied in the numerical analysis. In practice, sleeve friction is usually used for soil classification. For a further study, the effects of interface friction could be considered for varying roughnesses of the friction sleeve, together with the micropolar effects of soils. Further work is also needed to investigate the effects of other soil models with a more detailed comparison between the FE solutions and experimental data. Other existing analytical/numerical methods for CPT analysis could also be investigated.

References

- [1] Baligh MM. Strain path method. *ASCE J Soil Mech Found Div* 1985;111(9):1108–36.
- [2] Bolton MD. The strength and dilatancy of sands. *Géotechnique* 1986;36(1):65–78.
- [3] De Borst R, Vermeer PA. Finite element analysis of static penetration tests. *Géotechnique* 1984;34(2):199–210.
- [4] De Simone P, Golia G. Theoretical analysis of the cone penetration test in sands. In: *Proceedings of the 1st International Symposium on Penetration Testing*, 1988; vol. 2. p. 729–35.
- [5] Durgunoglu HT, Mitchell JK. Static penetration resistance of soils. I-II. In: *Proceedings of the ASCE Spec Conference on In Situ Measurement of Soil Properties*, 1975; vol. 1: p. 51–89.
- [6] Gupta RC. Finite element analysis for deep cone penetration. *ASCE J Geotech Eng* 1992;177(10):1610–30.
- [7] Herrmann LR, Mello J. Investigation of an alternative finite element procedure: a one-step, steady-state analysis. Report No. CR 95.001, Dept. of Civil and Environmental Eng., University of California at Davis, USA; 1994.
- [8] Hibbitt, Karlsson, Sorensen, Inc., ABAQUS theory manual, Version 6.2; 2001.
- [9] Houlsby GT, Wroth CP. Determination of undrained strengths by cone penetration tests. In: *Proceedings of the 2nd European Symposium on Penetration testing*, 1982; vol. 2. p. 585–90.
- [10] Houlsby GT, Wheeler AA, Norbury J. Analysis of undrained cone penetration as a steady flow problem. In: *Proceedings of the 5th International Conference on Numerical Methods in Geomechanics*, 1985; vol. 4. p. 1767–73.
- [11] Janbu N, Senneset K. Effective stress interpretation of in situ static penetration tests. In: *Proceedings of the 1st European Symposium on Penetration Testing*, 1974; vol. 2. p. 181–93.
- [12] Kioussis PD, Voyiadjis GZ, Tumay MT. A large strain theory and its application in the analysis of the cone penetration mechanism. *Int J Num Anal Meth, Geomech* 1988;12:45–60.
- [13] Ladanyi B, Johnson GH. Behaviour of circular footings and plate anchors embedded in permafrost. *Can Geotech J* 1974;11:531–53.
- [14] Lunne T, Robertson PK, Powell JJM. *Cone penetration testing in geotechnical practice*. London: Blackie; 1997.
- [15] Robertson PK, Campanella RG. Interpretation of cone penetration tests. I: Sand. *Can Geotech J* 1983;20:718–33.
- [16] Salgado R, Mitchell JK, Jamiolkowski M. Cavity expansion and penetration resistance in sand. *ASCE J Geotech Geoenv Eng* 1997;123(4):344–54.
- [17] Sheng, D, Axelsson, K, Magnusson, O. Stress and strain fields around a penetrating cone. In: *Proceedings of the 6th International Symposium on Numerical Models in Geomechanics – NUMOG-VI*, July 1997, Montreal, Canada, Balkema, Rotterdam, 1997; p. 456–65.
- [18] Van den Berg, P., 1994. Analysis of soil penetration. Ph.D. thesis, Delft University, The Netherlands.
- [19] Vesic AS. Expansion of cavities in infinite soil mass. *ASCE J soil Mech Found Div* 1972;98:265–90.
- [20] Vesic, A.S.. Design of pile foundations. National Cooperation Highway Research Program Report No. 42, Transaction Research Board, Washington, DC; 1977.
- [21] Wroth CP. The interpretation of in situ soil test. 24th Rankine Lecture. *Géotechnique* 1984;34(4):449–89.
- [22] Yu HS, Houlsby GT. Finite cavity expansion in dilatant soils: loading analysis. *Géotechnique* 1991;41(2):173–83.
- [23] Yu HS, Schnaid F, Collins IF. Analysis of cone pressuremeter tests in sands. *J Geotech Eng ASCE* 1996;122(8):623–32.
- [24] Yu HS, Mitchell JK. Analysis of cone resistance: a review of methods. *J Geotech Geoenv Eng ASCE* 1998;124(2):140–9.
- [25] Yu HS, Herrmann LR, Boulanger RW. Analysis of steady cone penetration in clay. *J Geotech Geoenv Eng ASCE* 2000;126(7): 594–605.